Enhanced solar water splitting using plasmon-induced resonance energy transfer and unidirectional charge carrier transport

HUAPING JIA,[1,2] YAT LAM WONG,[2] BINGZHE WANG,[3] GUICHUAN XING,[3] CHI CHUNG TSOI,[2] MEILING WANG,[1] WENDONG ZHANG,[1] AOQUN JIAN,[1,5] SHENGBO SANG,[1,6] DANGYUAN LEI,[4] AND XUMING ZHANG[2,7]

[1]*Micro Nano System Research Center, Key Lab of Advanced Transducers and Intelligent Control System of the Ministry of Education & College of Information and Computer, Taiyuan University of Technology, Taiyuan, 030024, China*
[2]*Department of Applied Physics, The Hong Kong Polytechnic University, Hong Kong, 999077, China*
[3]*Joint Key Laboratory of the Ministry of Education, Institute of Applied Physics and Materials Engineering, University of Macau, Macao, 999078, China*
[4]*Department of Materials Science and Engineering, City University of Hong Kong, Hong Kong, 999077, China*
[5]*jianaoqun@tyut.edu.cn*
[6]*sunboa-sang@tyut.edu.cn*
[7]*apzhang@polyu.edu.hk*

Abstract: Solar water splitting by photoelectrochemical (PEC) reactions is promising for hydrogen production. The gold nanoparticles (AuNPs) are often applied to promote the visible response of wideband photocatalysts. However, in a typical TiO_2/AuNPs structure, the opposite transfer direction of excited electrons between AuNPs and TiO_2 under visible light and UV light severely limits the solar PEC performance. Here we present a unique $Pt/TiO_2/Cu_2O/NiO$/AuNPs photocathode, in which the NiO hole transport layer (HTL) is inserted between AuNPs and Cu_2O to achieve unidirectional transport of charge carriers and prominent plasmon-induced resonance energy transfer (PIRET) between AuNPs and Cu_2O. The measured applied bias photon-to-current efficiency and the hydrogen production rate under AM 1.5G illumination can reach 1.5% and 16.4 $\mu mol \cdot cm^{-2} \cdot h^{-1}$, respectively. This work is original in using the NiO film as the PIRET spacer and provides a promising photoelectrode for energy-efficient solar water splitting.

1. Introduction

Solar energy conversion is an attractive and sustainable solution to energy and environmental risks [1–3]. In recent years, tremendous efforts have been devoted to solar-to-fuel energy conversion by using semiconductor photoelectrodes [4–6]. Photoelectrochemical (PEC) water splitting was first demonstrated in 1972 by irradiating TiO_2 with ultraviolet (UV) light to produce hydrogen, [4] and has since been regarded as a promising and environmentally method to obtain hydrogen in a sustainable manner [1]. The PEC efficiency relies heavily on the light absorption and the charge carrier generation/ separation/ transport/ recombination processes, which are in turn strongly determined by the photoelectrode design [7–9]. Among the various semiconducting materials used for solar energy conversion, TiO_2 has been intensively investigated and widely applied as photoelectrode for the PEC water splitting thanks to its high photochemical stability, non-toxicity, and low cost. However, the wide bandgap of TiO_2 (3.2 eV) limits its absorption to only the UV region of solar light, which takes up only 5% at maximum of the solar energy. Therefore, a major

challenge is to utilize the visible region of solar light so as to increase the efficiency of energy conversion.

One approach is to combine TiO_2 with narrow bandgap semiconductor materials to extend the light absorption of the photoelectrodes to the visible region [3]. Cuprous oxide (Cu_2O) is an attractive p-type oxide with a direct bandgap of 2 eV, which is suitable for capturing a large portion of the visible spectrum [10]. However, the poor stability of Cu_2O severely limits its use as a photocathode for water reduction [11,12]. Here we combine the chemical stability of TiO_2 as the surface protective layer [13] and the visible absorption of Cu_2O with their conveniently aligned band structure to form an n-TiO_2/p-Cu_2O heterojunction electrode. Furthermore, the development of surface plasmon resonance (SPR) in recent years has offered a new opportunity to overcome the limited efficiency of photocatalytic devices [14–16]. Incorporating noble metal nanostructures with semiconductors has become a common practice to enhance the photocatalytic activity in visible light mainly by three processes: (i) direct electron transfer (DET), (ii) local electromagnetic field enhancement (LEMF) and (iii) plasmon-induced resonant energy transfer (PIRET) [17–21].

For the typical TiO_2/Au nanoparticles (TiO_2/AuNPs) structure, the SPR-excited hot electrons of AuNPs under visible light overcome the Au-TiO_2 Schottky barrier to inject into the conduction band of TiO_2 in the DET process, while the electrons excited by the UV light in the TiO_2 layer may migrate to AuNPs due to the low Fermi-level energy of Au (see Fig. 1) [14,22–26]. This contradicting direction of electron transport would deteriorate the application of the SPR effect of AuNPs in solar water splitting. By combining the p-type narrow bandgap semiconductor Cu_2O with the TiO_2/AuNPs structure, here we consider a typical design of TiO_2/Cu_2O/AuNPs photoelectrode to extend the photocatalysis performance in the full spectrum. The formed p-n junction of TiO_2/Cu_2O may prevent the excited electrons in TiO_2 move back to AuNPs. But the excited electrons on the conduction band of Cu_2O may still drop to AuNPs partially in both visible and UV light [27]. In previous studies, the hole transport layer (HTL) was adopted under the Cu_2O layer to promote the charge carrier separation efficiency, or Au nanostructures were used as a plasmonic photosensitizer along with the Cu_2O layer to increases light harvesting [2,7,27–29]. However, no much effort is made to combine the HTL with the SPR effect of Au nanostructure in a single photoelectrode for solar water splitting.

Due to the absorption overlap between AuNPs and Cu_2O, there are three SPR effects (DET, LEMF, and PIRET) existing in the TiO_2/Cu_2O/AuNPs structure. The DET effect requires the direct contact of AuNPs with the semiconductor. The LEMF requires the photon energies to be higher than the bandgap of the semiconductor, and the AuNPs to be very close to the semiconductor (typically < 10 nm) to ensure the intense local electrical field regions (i.e., hotspots) of AuNPs has spatial overlaps with the semiconductor. In contrast, the PIRET process is a dipole-dipole interaction that needs some absorption overlap of AuNPs and the semiconductor, and enables to excite electron-hole pairs in the semiconductor at the energies below and near the band edge (i.e., the photon energy can be smaller the bandgap of semiconductor) [18,19,30,31]. It does not require direct contact or a very short distance between AuNPs and the semiconductor, and often allows the insertion of a thin insulating layer between AuNPs and the semiconductor (i.e., ref. 7 used a 100-nm thick Al_2O_3 layer). In previous research, NiO is considered as one of the most promising HTL for its high hole mobility and good stability [2]. Furthermore, due to its high conduction band position, it can block electron transport while allowing for hole transport when corporate with AuNPs [32].

In this work, we apply the NiO insulating layer between AuNPs and Cu_2O to propose a TiO_2/Cu_2O/NiO/AuNPs multilayered photocathode (see Fig. 1(c)). It incorporates multiple enhancement mechanisms into a single photoelectrode (see Figs. 1(d) and 1(e)), including (i) unidirectional transport of photoexcited carriers regulated by the NiO HTL under solar light, (ii) enhanced visible light absorption and photoexcitation of electron/hole pairs in the Cu_2O by
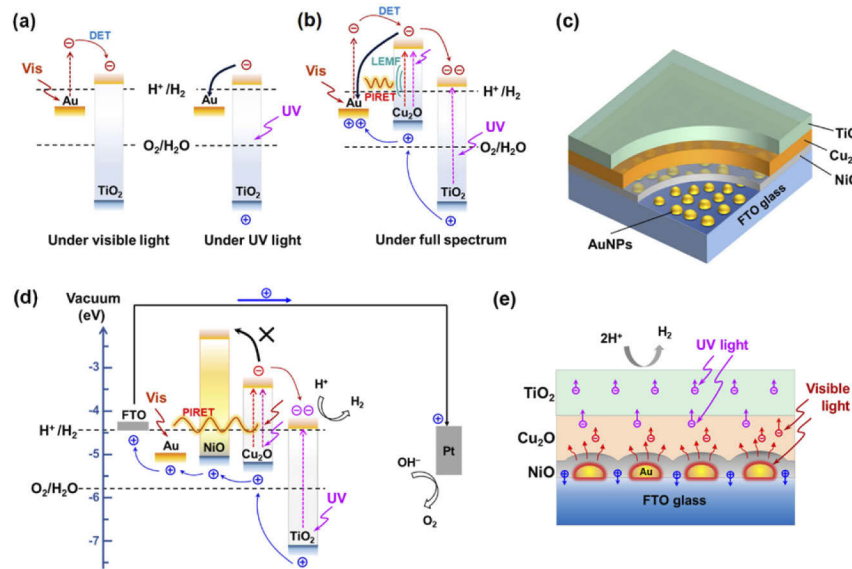
Fig. 1. (a) Band diagrams of TiO_2/AuNPs film under the irradiation of visible light (left) and UV light (right). (b) Band diagrams of TiO_2/Cu_2O/AuNPs film to elucidate the contradicting directions of electron transports under the full spectrum light. (c) 3D diagram and (d) working principle of our TiO_2/Cu_2O/NiO/AuNPs photocathode design for the full-spectrum water splitting, in which the NiO HTL plays the key role in regulating the direction of electron transport and acting as the spacer to enable the PIRET process as the same time. (e) The cross-sectional view of the layer structure to show the regulated transports of charge carriers under the irradiation of full spectrum light.

the prominent PIRET effect between Cu_2O and AuNPs, (iii) promoted electron-hole separation rate due to the p-n junction of TiO_2/Cu_2O heterostructure, (iv) isolation of Cu_2O and AuNPs by the TiO_2 protective layer from the electrolyte. As the Pt cocatalyst has been shown to provide the highest electrochemical activity toward hydrogen evolution reaction (HER), Pt nanoparticles are decorated on the sample surface to facilitate the catalytic reaction in hydrogen production measurement. This photoelectrode appears to be the first attempt to use the NiO thin film as the spacer for the PIRET effect between the AuNPs and the Cu_2O layer, and would provide a new concept to the PEC water splitting in solar light.

2. Experimental section

2.1. Preparation of TiO_2/Cu_2O/NiO/AuNPs

2.1.1. Preparation of AuNPs

First, the fluorine doped SnO_2 glass substrates (FTO) were cleaned using ultrasonication in acetone, ethanol, and deionized water for 10 minutes successively, and dried in the oven. Then, a thin Au film (8 nm thick) was deposited by E-beam system (JSD500 Electron Beam, JS Vacuum, Anhui, China). The evaporation rate was maintained at 0.01 nm/s under the pressure of about 4×10^{-6} Torr. Finally, the AuNPs were achieved after being annealed at 480 °C for 90 min in ambient atmosphere.

2.1.2. Preparation of NiO thin film

The Ni film was deposited by E-beam system (JSD500 Electron Beam, JS Vacuum, Anhui, China) and then annealed at 500 °C for 120 min to obtain a uniform NiO thin film.

2.1.3. Preparation of Cu$_2$O layer

The Cu$_2$O thin films were deposited by utilizing the DC reactive magnetron sputtering technique (Denton Explorer 14 Sputtering System) in a mixture of oxygen and argon (O$_2$:Ar = 6 sccm:40 sccm) at room temperature. The deposition chamber was evacuated to a base pressure of 4 × 10^{-6} Torr and the sputtering power was set to be 60 W.

2.1.4. Preparation of TiO$_2$ film

The TiO$_2$ protective layer was deposited by Atomic Layer Deposition (ALD, Ultratech) at 150 °C. The precursors with Tetrakis (dimethyl amido) titanium (IV) and H$_2$O were dosed for 0.1 s and 0.015 s, separately, followed by a 5 s nitrogen purge after each dose. The process consisted of 638 cycles (deposition rate 0.47 Å/cycle).

2.1.5. Preparation of Pt cocatalyst

The Pt nanoparticles on the surface of TiO$_2$ layer were prepared by an electrochemical deposition method. The prepared electrode samples were capsulated by epoxy and then immersed in 0.5 mM H$_2$PtCl$_6$ electrolyte to form an electrochemical deposition device at a current density of -8.5 μA·cm^{-2} for 15 min.

2.2. Sample characterizations

The scanning electron microscopy (SEM) images were taken using a field emission scanning electron microscope (FE-SEM, Tescan MAIA3). Optical absorption measurements of the prepared samples were measured by a Perkin-Elmer Lambda (950 UV/vis/NIR) spectrophotometer with the integrated sphere. Crystallinity and phase orientations of the samples were determined by the XRD technique measured with Cu KR radiation source (λ = 1.54 Å) under the accelerating voltage of 40 kV and the current of 40 mA with a normal 2θ scan. X-ray Photoelectron Spectroscopy (XPS) analysis of the samples was carried out using Nexsa X-Ray Photoelectron Spectrometer System with an Al Kα X-ray source (E = 1486.6 eV). The binding energy was calibrated using the C 1s photoelectron peak at 284.6 eV as the reference. Transient absorption (TA) measurements were performed by using the Ultrafast System HELIOS TA spectrometer at room temperature. The laser pulse was from Coherent Astrella-1K-F Ultrafast Ti: Sapphire Amplifier (<100 fs, 1 kHz). The broadband probe pulses (400-800 nm) were induced by focusing a small portion of the fundamental 800 nm laser pulses into an Al$_2$O$_3$ plate, and the pump pulses (500 nm) were generated from a Light Conversion TOPAS-C optical parametric amplifier.

2.3. Finite-difference time-domain simulation

The finite-difference time-domain (FDTD) method (Lumerical Solutions) was employed to analyze the optical response of the nanostructure. The simulated AuNPs layer was set to be randomly dispersed semi-spheres on the FTO substrate and the size of AuNPs was chosen to follow the measured histogram of particle size distributions. The NiO, Cu$_2$O, and TiO$_2$ layers were set according to the thicknesses of the samples using in experiments. In the simulation, the polarization of the E-field was set along the *X* axis and the propagation direction of light was set along the *Z* axis. The periodic boundary conditions were applied along the *X* and *Y* axes. To attain convergence, a Perfectly Matched Layer (PML) condition was applied on the positive side of Z-axis, at 600 nm above and below the (x, y, 0) surface. Hence, the total length of the simulation region along the *Z*-axis was 1200 nm. A plane wave was launched downward from 450 nm below the upper PML. For the simulation of the single AuNP on the FTO substrate, the diameter of AuNP was set to be 35 nm and other material properties remained the same as above. The dielectric functions of NiO, Cu$_2$O, and TiO$_2$ used for simulation are adopted from previous research [33–35].

2.4. *Photoelectrochemical measurements*

The photocatalytic reaction was measured with an electrochemical workstation (CHI 660E, Shanghai Chenhua Co., Ltd. China) in a standard three-electrode configuration containing a saturated Ag/AgCl as the reference electrode and a Pt wire as a counter electrode. The measurements were made in an electrolyte solution of 0.5 M Na_2SO_4 (pH = 6.8). The potential in this manuscript was referred to the RHE using the following equation:

$$E(vs.RHE) = E(vs.Ag/AgCl) + 0.197 + 0.0591 * pH \qquad (1)$$

The linear sweep voltammetry (LSV) mode was scanned at a rate of 10 mV/s. The photocurrent was measured under chopped illumination, therefore the dark and light currents could be monitored simultaneously. The incident-photon-to-current efficiency (IPCE) was carried out on the same three-electrode cell. The photocurrent was recorded with a spectral step of 10 nm by a monochromator (Newport Corp.). The IPCE value was calculated by using the following equation:

$$IPCE = \frac{I(A/cm^2)}{P(W/cm^2)} \times \frac{1240}{\lambda(nm)} \times 100\% \qquad (2)$$

where I. the photocurrent (A/cm^2), P. the intensity of incident monochromatic light at a specific wavelength (W/cm^2), and λ. the incident light wavelength (nm).

2.5. *Hydrogen production measurement*

Hydrogen quantification is conducted in an outer irradiation-type photoreactor which was connected to a closed gas-circulation system (Labsolar-III Beijing Perfectlight Technology Co. Ltd, China). It was measured in an electrolyte solution of 0.5 M Na_2SO_4 buffered with 0.1 M NaH_2PO_4 to obtain pH = 5. The GC 7900 system was calibrated by using high-purity hydrogen standards and was subsequently used to quantify the amount of hydrogen liberated under experimental conditions. The whole system was pumped out with a vacuum pump before the reaction to remove the dissolved air. The temperature for all photocatalytic reactions was kept at about 5 °C. Under the irradiation of the Xe arc lamp, the amount of hydrogen evolved was recorded by an on-line gas chromatograph (GC-7900, TCD detector) in which N_2 was used as the carrier.

3. Results and discussion

3.1. *Structural and composition characterizations*

The layer structure of our $TiO_2/Cu_2O/NiO/AuNPs$ photoelectrode is illustrated in Fig. 1(c). The photoelectrode starts with an AuNPs layer deposited directly on the surface of FTO substrate, which is then covered by a NiO thin film (15 nm thick). Next, a Cu_2O layer (30 nm thick) and a TiO_2 overlayer (30 nm thick) are grown on the top successively. The working mechanism of our $TiO_2/Cu_2O/NiO/AuNPs$ photoelectrode is illustrated in Fig. 1(d) and Fig. 1(e) for the photocatalytic water splitting under the full spectrum of solar light. Under the visible region of solar light, the AuNPs enable strong absorption by the localized surface plasmon resonance (LSPR) and excites hot electrons inside itself and intense electric field nearby. However, the NiO thin film has a higher conduction band minimum (-1.8 eV) than the Cu_2O layer (-3.3 eV) at vacuum level, and prevents the transport of hot electrons from the AuNPs to the Cu_2O layer, i.e., it avoids the DET [36,37]. The NiO film in this work is chosen to be 15 nm thick (optimized for photocurrent by experiments, see Figure S6 and the discussion below), which is too thick to extend the AuNPs hotspots into the Cu_2O layer (see Figure S4 and the discussion below) but still short enough for the PIRET process. By rational design of the layer structure and proper choices of the layer parameters, we can rule out the DET and the LEMF to utilize only the PIRET effect.

As further shown in Fig. 1(d), the Cu_2O layer can utilize both the UV and visible lights by its direct bandgap absorption to excite electrons and holes. Since the conduction band of Cu_2O is situated far below that of NiO but still higher than that of TiO_2, the conduction-band electrons in Cu_2O can move only from Cu_2O to TiO_2 [38]. Moreover, the TiO_2 overlayer can absorb UV light and excite the electron-hole pairs as well. As the valance band of TiO_2 is lower than that of Cu_2O, the photo-excited holes flow from TiO_2 to Cu_2O and further through NiO and AuNPs to the FTO substrate eventually. This shows that the use of NiO film ensures the unidirectional transport of electrons from Cu_2O to the TiO_2 film while the holes are always transported towards the FTO substrate. Therefore, under either visible light or UV light, the transport direction of photo-excited electrons (or holes) remains no change, and the photocurrent under visible light always adds up constructively with that under UV light. In the other words, the unidirectionality of the electron and hole transport enables the constructive use of both the visible and UV regions of solar light for the PEC water splitting.

The scanning electron microscopic (SEM) images in Figs. 2(a) – 2(e) show the morphologies of the prepared AuNPs sample, the NiO/AuNPs bilayer, the Cu_2O/NiO/AuNPs trilayer and the TiO_2/Cu_2O/NiO/AuNPs multilayer, all on the FTO substrate. The AuNPs sample is fabricated by the annealing of a sputtered thin Au film (8 nm thick). The size of AuNPs varies between 20–55 nm with the average of 35 nm (see the histogram in the inset of Fig. 2(a)). With the deposition of the NiO film (15 nm thick) on top of the AuNPs, the NiO/AuNPs bilayer shows large but random blocks (see Fig. 2(b)). After the further deposition of the Cu_2O layer (30 nm thick), it exhibits closely-packed large particles (see Fig. 2(c)). With the subsequent deposition of TiO_2 overlayer, the morphology remains similar due to the conformal feature of atomic layer deposition (ALD) deposition (see Fig. 2(d)). As seen from the pseudo-color cross-sectional SEM of the TiO_2/Cu_2O/NiO/AuNPs multilayer in Fig. 2(e) (see Figure S1 for the original grayscale image), the TiO_2 and Cu_2O layers completely cover the NiO/AuNPs bilayer, which is beneficial to both the transport of charge carriers and the prevention of photocorrosion/leaching.

The crystalline phases of the samples are analyzed by the X-ray diffraction (XRD) (Fig. 2(f)). The peaks at 2θ. 38.18°, 44.39°, 64.58° and 77.55° identify the crystal planes of Au (JCPDS file no. 04-0784). The characteristic peaks appear at 37.3°, 43.3° and 62.9° belonging to the (111), (200), and (220) crystal planes of NiO (JCPDF: 44-1159), respectively. The diffraction peaks located at 37.01°, 42.61° and 62.44° are indexed to the (111), (200) and (220) crystal planes of Cu_2O (JCPDS 34-1354), respectively. Since the TiO_2 layer is deposited by the ALD method at 100°C, it shows the amorphous phase. In the XRD pattern of the TiO_2/Cu_2O/NiO/AuNPs multilayer on the FTO substrate, the peaks associated with the constituent material are retained, the reduced intensity of Au compared with the standalone AuNPs may be due to the burial of the AuNPs at the bottom.

The X-ray photoelectron spectroscopy (XPS) technique is employed to analyze the elemental valence state of the samples. Figure S2a shows the wide-scan XPS spectra of TiO_2/Cu_2O heterostructure. The peaks at 458.1 and 463.8 eV in Figure S2b belong to Ti $2p_{3/2}$ and Ti $2p_{1/2}$, indicating the existence of Ti (IV) oxide in the TiO_2/Cu_2O heterostructure. Figures S2c and S2d show the XPS spectra of Cu $2p$ and O $1s$ with and without the TiO_2 deposition. The two peaks at 932.08 eV and 951.78 eV in Figure S2c for both TiO_2/Cu_2O and bare Cu_2O are assigned to Cu $2p_{3/2}$ and Cu $2p_{1/2}$ of Cu^+, respectively [3,39]. This indicates that the Cu_2O nanocrystals are formed successfully and the process of TiO_2 coating does not affect the state of the Cu_2O underneath. The O $1s$ spectra in Figure S2d exhibit peaks at 529.58, 530.08, 531.58 eV for TiO_2/Cu_2O, and 530.38, 531.38 eV for the bare Cu_2O layer, showing different chemical states of oxygen.
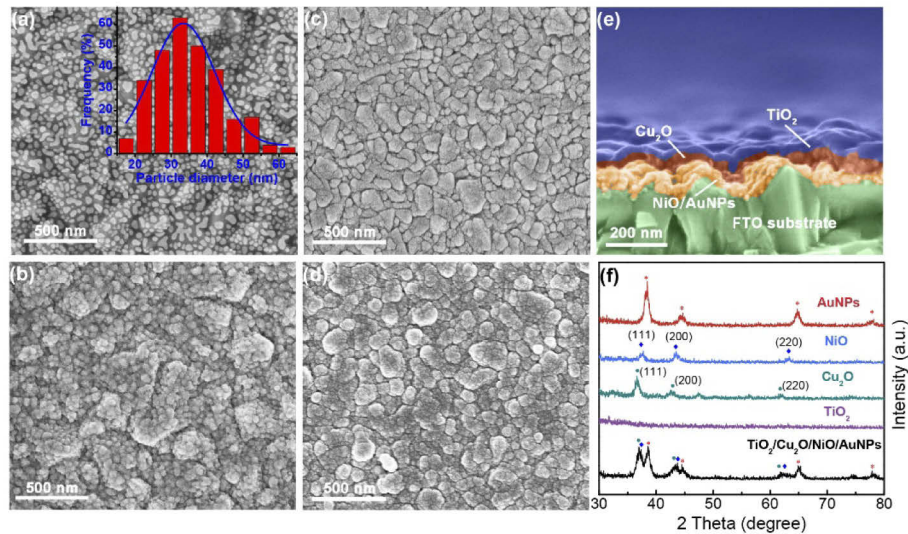
Fig. 2. Scanning electron micrographs (SEMs) of (a) AuNPs, (b) NiO/AuNPs, (c) Cu$_2$O/NiO/AuNPs, (d) TiO$_2$/Cu$_2$O/NiO/AuNPs, and (e) pseudocolor cross-section of the TiO$_2$/Cu$_2$O/NiO/AuNPs multilayer on the FTO substrate. The thicknesses of the Cu$_2$O layer and the TiO$_2$ overlayer are both about 30 nm. The thickness of NiO film is 15 nm. (f) XRD patterns of AuNPs, NiO, Cu$_2$O, TiO$_2$ and TiO$_2$/Cu$_2$O/NiO/AuNPs on the FTO substrate. In (a), the inset shows the histogram of the AuNPs size, which varies between 20–55 nm with the average of 35 nm.

3.2. Optical properties

The UV-vis spectra over the range of 250–750 nm are measured to characterize the optical absorptions of the samples. As shown in Fig. 3(a), the bare TiO$_2$ film (30 nm thick) has a decreasing absorption from 250 to 370 nm and drops to a very low level afterward. The addition of an underlying Cu$_2$O layer (30 nm thick) enhances the absorption over the whole wavelength range. More specifically, the absorption over 250–550 nm is mainly due to the interband absorption of Cu$_2$O while the absorption at $\lambda > 550$ nm is attributed to the intraband absorption of Cu$_2$O [40,41]. With the addition of buried AuNPs, the resulted TiO$_2$/Cu$_2$O/AuNPs trilayer further increases the absorption over the whole wavelength range with broad absorption peaks near 370 nm and 730 nm. The enhancement of absorption in visible light may be attributed to the strong SPR effects caused by AuNPs [28]. By inserting a NiO thin film (15 nm thick) between the AuNPs and the Cu$_2$O layer, the TiO$_2$/Cu$_2$O/NiO/AuNPs multilayer has higher absorption than TiO$_2$/Cu$_2$O/AuNPs, and the second peak is shifted to 670 nm. Since the 15-nm NiO film itself has a high transmittance (>80%) (see Figure S3), it allows most of the visible light to reach AuNPs when the irradiation is from the TiO$_2$ side of the sample.

To further examine the nature of plasmon modes, we calculated and analyzed the absorption spectra and the electric-field enhancements of TiO$_2$/Cu$_2$O/NiO/AuNPs by using the finite difference time domain (FDTD) method based on the experimentally determined particle size distribution in SEM images (see the inset of Fig. 2(a)). From Fig. 3(b), it is shown that the simulated absorption spectrum well resembles the measured one in the aspects of the curve shape and the peak positions (e.g., the simulated peak at 685 nm). The influences of individual layers are also simulated as shown in Fig. 3(c). The comparison of the absorption spectrum of AuNPs and NiO/AuNPs shows that the NiO thin film results in an increase in the intensity of the plasmon absorption and a red shift of the LSPR peak position (from 612 to 670 nm). And the absorption
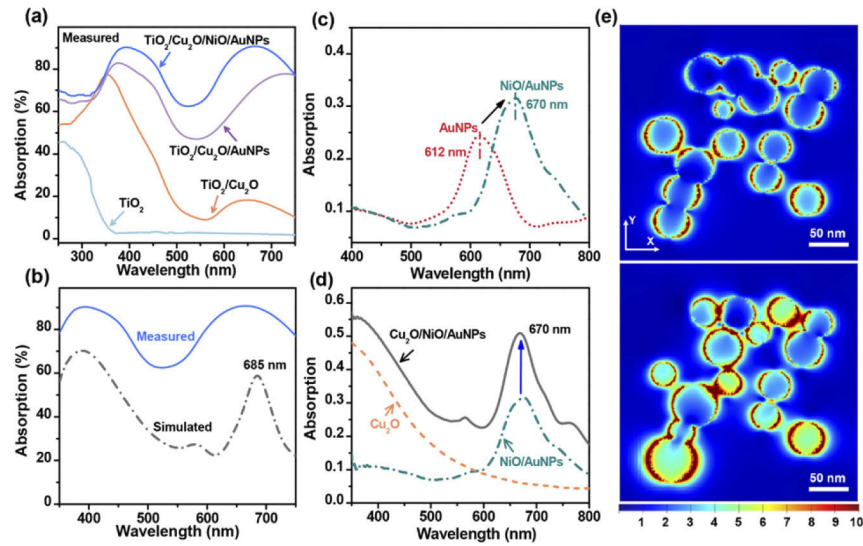
Fig. 3. (a) The measured UV-vis absorption spectra of TiO_2, TiO_2/Cu_2O, $TiO_2/Cu_2O/AuNPs$, and $TiO_2/Cu_2O/NiO/AuNPs$, all on the FTO substrate. (b) The measured and simulated absorption spectra of the $TiO_2/Cu_2O/NiO/AuNPs$ multilayer on the FTO substrate. Simulated absorption spectra of (c) AuNPs and NiO/AuNPs; and (d) Cu_2O, NiO/AuNPs, and $Cu_2O/NiO/AuNPs$. (e) Simulated electric field intensities (top view) of only AuNPs at the plasmonic resonance wavelength 612 nm (upper image) and $TiO_2/Cu_2O/NiO/AuNPs$ at its own plasmonic resonance wavelength 685 nm (lower image). The color scale bar shows the relative increase in field enhancement $|E|/|E_0|$. The regions of hot spots of $TiO_2/Cu_2O/NiO/AuNPs$ is larger than that of only AuNPs. In (a) – (d), measured data are shown in solid lines, and simulated results are shown in dashed, dotted or dash-dotted lines.

of $Cu_2O/NiO/AuNPs$ trilayer in most of the wavelength range is merely a summation of those of the bare Cu_2O layer and the NiO/AuNPs bilayer (see Fig. 3(d)). Nevertheless, some extra increase of absorption at the plasmonic peak near 670 nm is prominent, suggesting the extra contribution from the PIRET effect (that is, the absorption of $Cu_2O/NiO/AuNPs$ trilayer near 670 nm results from the absorption of Cu_2O, the LSPR absorption of AuNPs and additionally the PIRET effect of AuNPs to Cu_2O). As shown in Fig. 3(e), the simulated electric field intensity of $TiO_2/Cu_2O/NiO/AuNPs$ at the plasmonic peak of 685 nm (see the lower image) is significantly enhanced and has a much larger hot spot than that of AuNPs at its LSPR peak of 612 nm (see the upper image).

In addition, we simulated a single AuNP covered successively by the NiO thin film (15 nm thick) and the Cu_2O layer (30 nm thick) to investigate the change of electric field. As shown in Figure S4a, the plasmonic absorption peaks of AuNP, NiO/AuNP and $Cu_2O/NiO/AuNP$ are calculated to be at 623, 678, and 684 nm, respectively. The $Cu_2O/NiO/AuNP$ has an enhanced absorption at the plasmonic peak 684 nm, apparently higher than NiO/AuNP at 678 nm. This extra increase of absorption may be because the AuNPs non-radiatively transfers the energy to the Cu_2O layer by the PIRET effect and reduces the scattering. Figure S4b, Figure S4c and Figure S4d present the electric field distributions of AuNP, NiO/AuNP and $Cu_2O/NiO/AuNP$ at their own plasmonic absorption peaks. Due to the high refractive index of NiO insulator, the hot spot regions of NiO/AuNP are obviously larger than those of the single AuNP. With the addition of the Cu_2O layer, the $Cu_2O/NiO/AuNP$ sample has the similar spatial distribution of local electric field to that of NiO/AuNP (see Figures S4 (c2), (c3), (d2), (d3)). In the other word,

the Cu_2O layer of the Cu_2O/NiO/AuNP sample does not have the plasmon-enhanced electric field. Therefore, the LEMF effect is not a major factor. It is noted that the FDTD simulates only the electromagnetic field near the AuNPs. To further investigate the PIRET effect from AuNPs to the dipole of electron/hole pairs in Cu_2O, we performed the TA spectroscopic measurements of the samples.

3.3. Transient absorption spectroscopy

The dynamics of primary photo-induced processes (e.g., recombination, charge transfer and trapping) can be studied in great detail using the ultrafast TA spectroscopy techniques [42]. As shown in Fig. 4(a), the TA spectrum of Cu_2O/AuNPs features a positive absorption band near 500–620 nm and a negative absorption band in 625–680 nm. While the bare Cu_2O film only has a positive absorption band in 500–680 nm (see Figure S5). Here the transient negative absorption is due to the plasmon bleaching of buried AuNPs [43]. It is further found that after the insertion of the NiO thin layer between Cu_2O and AuNPs, the negative absorption band of Cu_2O/NiO/AuNPs in Fig. 4(b) has a blue shift.
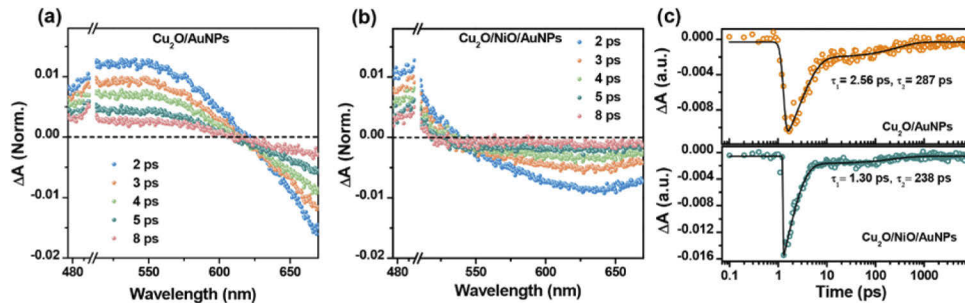

Fig. 4. Transient absorption spectra of (a) Cu_2O/AuNPs and (b) Cu_2O/NiO/AuNPs at different time delays under excitation of 500 nm laser pulses. (c) The bleaching kinetics and the relative fits of Cu_2O/AuNPs and Cu_2O/NiO/AuNPs at 650 nm.

Furthermore, the decay time τ was extracted by fitting the experimental data with a bi-exponential decay function as displayed in Fig. 4(c). The decay time τ_1 and τ_2 are related to the electron-phonon scattering process and the charge recombination process, respectively. By comparison, the shorter lived exciton state of Cu_2O/NiO/AuNPs ($\tau_1 = 1.30$ ps, $\tau_2 = 238$ ps) than Cu_2O/AuNPs ($\tau_1 = 2.56$ ps, $\tau_2 = 287$ ps) is due to the two factors: (i) the decay of plasmons in AuNPs is more prominent in Cu_2O/NiO/AuNPs via the PIRET from AuNPs to Cu_2O, (ii) the NiO spacer is efficient for the hole transfer from the Cu_2O layer to the AuNPs, which make the AuNPs just as a hole sink [44]. In addition, the lifetime of created carriers in the second process for Cu_2O/AuNPs and Cu_2O/NiO/AuNPs is derived on the order of a few hundred picoseconds, which corresponds with the interband recombination in previous research [18].

3.4. PEC performance

Since Cu_2O and AuNPs are the base materials, we first measured the photocurrents of the Cu_2O layer and the Cu_2O/AuNPs bilayer with a varying bias voltage under the chopped illumination of visible light (λ. 420 nm). As shown in Fig. 5(a), the response curves exhibit a typical p-type semiconductor behavior, i.e., acting as the photocathodes. The photocurrent density of the Cu_2O/AuNPs sample is higher than the pure Cu_2O sample. From the *i-t* curves in Fig. 5(b), the current density of Cu_2O/NiO/AuNPs trilayer is -82 $\mu A \cdot cm^{-2}$ at 0.3 V vs RHE (reversible hydrogen electrode), which is about 2.4 times of that of pure Cu_2O (-34 $\mu A \cdot cm^{-2}$) and 1.7 times of that of Cu_2O/AuNPs (-49 $\mu A \cdot cm^{-2}$). It is convincing that the AuNPs and NiO are

beneficial to the visible response of Cu_2O. Here the optimal thickness of NiO is 15 nm based on the experimental study shown in Figure S6. We varied the NiO thickness from 5 to 25 nm and obtained the highest magnitude of current density at 15 nm. This agrees with the observation in the reported work that an appropriate NiO thin film would enhance the interfacial charge transfer for HER [45].
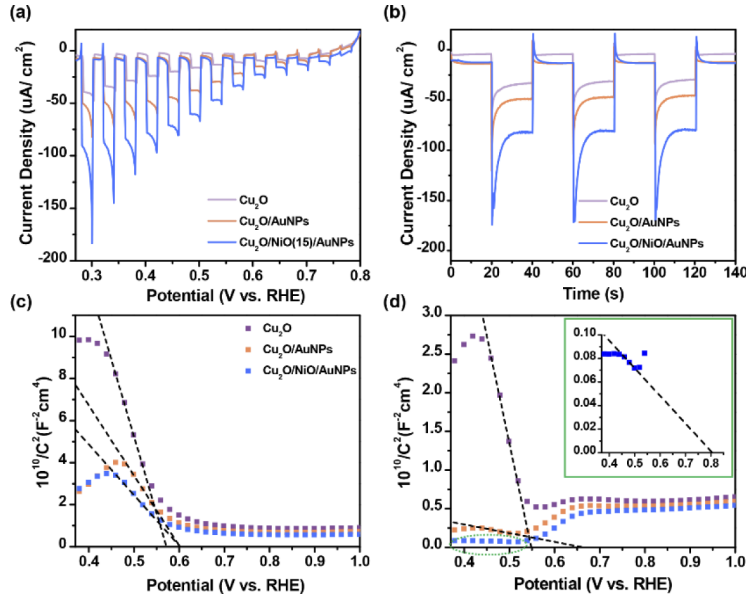
Fig. 5. (a) Linear sweep voltammetry and (b) the current densities of Cu_2O, $Cu_2O/AuNPs$ and $Cu_2O/NiO/AuNPs$ on the FTO substrate. The Mott-Schottky plots of Cu_2O, $Cu_2O/AuNPs$ and $Cu_2O/NiO/AuNPs$ were measured under dark (c) and visible light (d). The inset of (d) shows the enlarged view of the region as indicated by the green dashed circle.

Moreover, the density of charge carriers participating the PEC reactions can be evaluated by Mott−Schottky analysis. The Mott−Schottky plots were measured in the 0.5 M Na_2SO_4 electrolyte at 1 kHz with an amplitude of 5 mV under dark (see Fig. 5(c)) and visible light (see Fig. 5(d)). The linear fits to the Mott−Schottky plots have a negative slope associated with the p-type behavior and the charge carrier density can be calculated by the Mott−Schottky equation

$$\frac{1}{C^2} = \left(\frac{2}{e\varepsilon\varepsilon_0 N_d}\right)\left(V - V_{FB} - \frac{k_B T}{e}\right) \tag{3}$$

where C is the capacitance, e is the electron charge ($e = -1.6 \times 10^{-19}$ C), ε is the dielectric constant ($\varepsilon = 7.6$ for Cu_2O), ε_0 is the vacuum permittivity ($\varepsilon_0 = 8.86 \times 10^{-12}$ F·m^{-1}), N_d is the carrier density, V_{FB} is the flat-band potential, k_B is the Boltzmann constant, and T is the temperature. From the slope k of the C^{-2} vs V plot in Figs. 5(c) and 5(d), N_d can be calculated as 2.50×10^{17}, 5.63×10^{17}, and 7.73×10^{17} cm^{-3} in dark and 6.68×10^{17}, 1.66×10^{19}, and 7.90×10^{19} cm^{-3} in visible light for pure Cu_2O, $Cu_2O/AuNPs$ and $Cu_2O/NiO/AuNPs$, respectively. The carrier density relationship of the samples follows the trend: $Cu_2O/NiO/AuNPs > Cu_2O/AuNPs > Cu_2O$. This trend is the same as that of photocurrent densities in Fig. 5(b), indicating that a higher carrier density is beneficial to the PEC performance [46,47]. In addition, the considerable improvement of carrier density for $Cu_2O/NiO/AuNPs$ under illumination demonstrates that the electrons and holes are separated efficiently by applying the NiO HTL.

To alleviate the electrochemical corrosion of Cu_2O and to better utilize the solar light, a TiO_2 overlayer (30 nm thick) is applied on top of the Cu_2O layer by the ALD method. Here the p-type Cu_2O layer and the n-type TiO_2 layer naturally forms a p-n heterojunction. To investigate the influence of TiO_2 overlayer on the stability of photoelectrode, we measured and compared the photocurrents of the bare Cu_2O sample and the TiO_2/Cu_2O heterojunction. As shown in Figure S7, the photocurrent of the bare Cu_2O sample presented a fast and significant drop compared with that of the TiO_2/Cu_2O heterojunction. By using the exponential fitting, we can find that the mean lifetime of TiO_2/Cu_2O is ~2.3 times of that of Cu_2O, but the drop range of TiO_2/Cu_2O is only 1/3 of that of Cu_2O. In addition, the Tafel polarization curves were measured to analyse the corrosion of electrodes (see Figure S8). The photocorrosion current density for Cu_2O and TiO_2/Cu_2O were calculated to be 14.63 $\mu A \cdot cm^{-2}$ and 5.23 $\mu A \cdot cm^{-2}$ in 0.5M Na_2SO_4 under the AM 1.5G. The improved stability and lower corrosion current density of TiO_2/Cu_2O verify that the TiO_2 overlayer can protect the underlying Cu_2O layer to some extent.

After the deposition of TiO_2 overlayer, the IPCE values of TiO_2/Cu_2O, $TiO_2/Cu_2O/AuNPs$, and $TiO_2/Cu_2O/NiO/AuNPs$ are measured in the UV region and the visible region (see Fig. 6(a)). $TiO_2/Cu_2O/NiO/AuNPs$ performs the best in both UV and visible light regions. However, the UV region shows $TiO_2/Cu_2O/AuNPs$ < TiO_2/Cu_2O but the visible region has the opposite relationship of TiO_2/Cu_2O < $TiO_2/Cu_2O/AuNPs$. It indicates that the addition of AuNPs is unfavorable to the UV response but beneficial to the visible response. In contrast, the introduction of NiO film is beneficial to the IPCE value in both the UV and visible light regions.
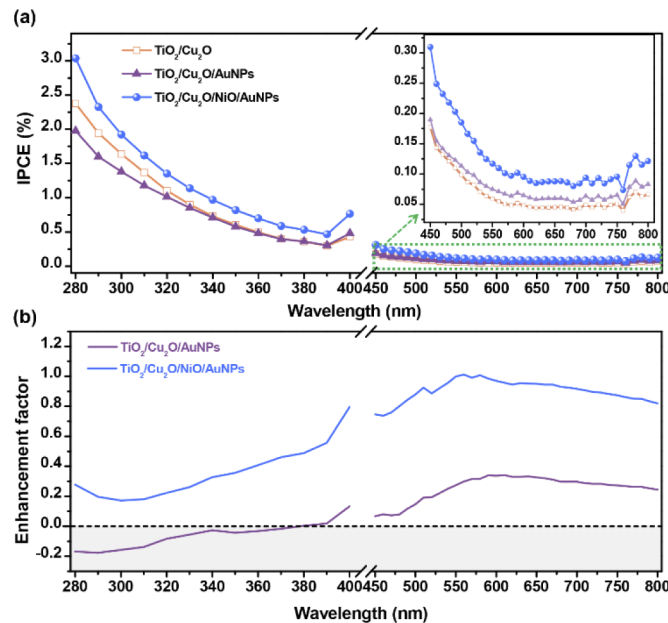
Fig. 6. (a) The measured incident-photon-to-current efficiency (IPCE) of TiO_2/Cu_2O, $TiO_2/Cu_2O/AuNPs$, and $TiO_2/Cu_2O/NiO/AuNPs$. The inset of (a) shows the enlarged view of the visible light region as indicated by the green dashed rectangle. (b) The enhancement factors of $TiO_2/Cu_2O/AuNPs$ and $TiO_2/Cu_2O/NiO/AuNPs$ with respect to TiO_2/Cu_2O. All photoelectrodes are measured in the 0.5 M Na_2SO_4 solution.

To quantify the beneficial effects of the AuNPs and the NiO thin film, we calculate the enhancement factor of $TiO_2/Cu_2O/AuNPs$ and $TiO_2/Cu_2O/NiO/AuNPs$ with respect to TiO_2/Cu_2O

using the expression:

$$\text{Enhancement factor} = \frac{\text{IPCE - IPCE}_{\text{TiO}_2/\text{Cu}_2\text{O}}}{\text{IPCE}_{\text{TiO}_2/\text{Cu}_2\text{O}}} \tag{4}$$

As shown in Fig. 6(b), the enhancement factor of $TiO_2/Cu_2O/AuNPs$ is below zero in the UV region, which might be because AuNPs could act as the electron-hole recombination center [24,48]. By covering the NiO thin film on the AuNPs to form the $TiO_2/Cu_2O/NiO/AuNPs$ multilayer, the excited electrons from Cu_2O cannot transfer back to AuNPs, only holes can transfer through the NiO thin film to the AuNPs and then to the FTO substrate, avoiding the recombination problem. Here, the AuNPs also acts as a fast lane to transfer the holes to the FTO substrate as its conductivity is much better than the bare FTO substrate. In the visible light region, both $TiO_2/Cu_2O/AuNPs$ and $TiO_2/Cu_2O/NiO/AuNPs$ present a positive enhancement factor since the AuNPs has the plasmonic effect in visible light. The enhancement factors of $TiO_2/Cu_2O/AuNPs$ and $TiO_2/Cu_2O/NiO/AuNPs$ have the maximum values of ~0.34 and 1.0, respectively. The NiO film itself (i.e., without AuNPs) can promote the separation rate of electron-hole pairs in the TiO_2/Cu_2O heterojunction, [32,49] and the enhancement factor is measured to have the maximum of ~0.37 (see Figure S9). It is interesting to see that the enhancement factor of $TiO_2/Cu_2O/NiO/AuNPs$ is larger than the summation of those of $TiO_2/Cu_2O/AuNPs$ and $TiO_2/Cu_2O/NiO$ (namely, $1.0 > (0.34 + 0.37) = 0.71$), suggesting certain synergy of the PIRET effect and the NiO HTL effect.

The photocurrent densities of TiO_2, TiO_2/Cu_2O, $TiO_2/Cu_2O/$ AuNPs and $TiO_2/Cu_2O/NiO/AuNPs$ measured under AM 1.5G are shown in Figure S10. It is obvious that the $TiO_2/Cu_2O/NiO/AuNPs$ shows the largest current density. Furthermore, the electrochemical impedance spectroscopy (EIS) is a powerful tool to evaluate the charge-transfer resistance across the electrode-electrolyte interface. Figure S11 shows the Nyquist plots of TiO_2, TiO_2/Cu_2O, $TiO_2/Cu_2O/$ AuNPs and $TiO_2/Cu_2O/NiO/AuNPs$ measured in 0.5 M Na_2SO_4 electrolyte under dark. It is noted that the semicircle in the Nyquist plot at high frequencies is a signature of the charge-transfer process and its radius represents the charge-transfer resistance [50,51]. The $TiO_2/Cu_2O/NiO/AuNPs$ shows the lowest charge transfer resistance due to the efficient charge transfer across the interface. This can also explain its best IPCE performance as shown in Fig. 6.

### 3.5. PEC hydrogen evolution performance

The hydrogen evolution of the $TiO_2/Cu_2O/NiO/AuNPs$ photocathode is investigated to evaluate their photocatalytic activity under AM 1.5G. As it is well known, Pt nanoparticles are commonly adopted as an effective hydrogen evolution co-catalyst due to the high work function [52,53]. In this study, we incorporate the same idea to decorate the Pt nanoparticles onto the surface of the samples in the hydrogen production measurement. The presence of Pt nanoparticles can reduce the reaction overpotential and decrease the interface barrier for the electrons transfer. Since the TiO_2 overlayer covers and protects the Cu_2O layer, it allows to use the electrolyte (pH = 5) that contains 0.5 M Na_2SO_4 and 0.1 M NaH_2PO_4.

The LSV curves of Pt/TiO_2, $Pt/TiO_2/Cu_2O$, $Pt/TiO_2/Cu_2O/AuNPs$, $Pt/TiO_2/Cu_2O/NiO$, and $Pt/TiO_2/Cu_2O/NiO/AuNPs$ were recorded under the chopped light of AM 1.5G illumination (see Fig. 7(a)). The $Pt/TiO_2/Cu_2O/NiO/AuNPs$ multilayer shows a photocurrent close to -1.44 mA·cm^{-2} at -0.18 V vs. RHE, which is 1.4, 2.1, 4.1 and 8.2 times of those of $Pt/TiO_2/Cu_2O/AuNPs$, $Pt/TiO_2/Cu_2O/NiO$, $Pt/TiO_2/Cu_2O$, Pt/TiO_2, respectively. Applied bias photon-to-current efficiency (ABPE) is an important figure of merit to measure the PEC water-splitting performance of a semiconductor photoanode as defined by,

$$\text{ABPE} = \frac{|I|(1.23 - |V_{\text{bias}}|)}{P_{\text{light}}} \times 100\% \tag{5}$$

where V_{bias} is the applied bias versus RHE, I is the measured current density, and P_{light} is the power density of the illumination. Figure 7(b) plots the calculated ABPEs from the results of Fig. 7(a) and shows that the Pt/TiO$_2$/Cu$_2$O/NiO/AuNPs multilayer gives the highest ABPE of 1.5%.
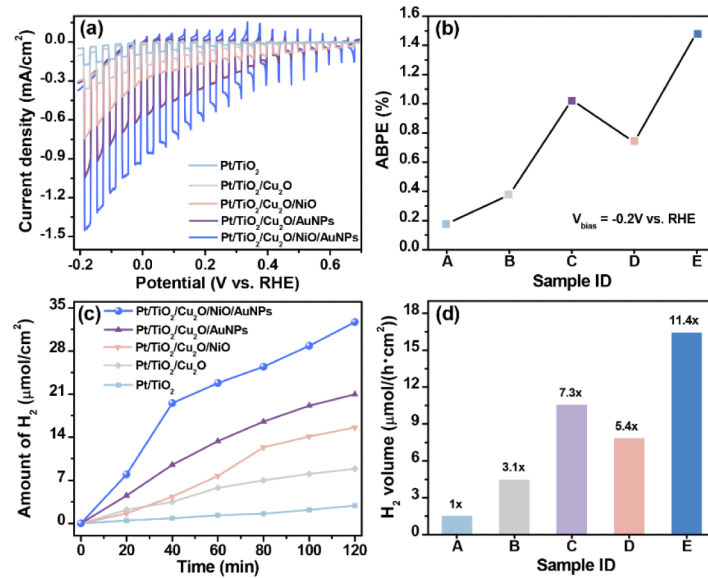
Fig. 7. (a) Linear sweep voltammetry (LSV) scanning curves, (b) applied bias photon-to-current efficiency (ABPE), (c) hydrogen yield, and (d) hydrogen production rate of the different photocathode samples. In (b) and (d), the sample IDs A-E represent the samples of Pt/TiO$_2$ (i.e., sample A), Pt/TiO$_2$/Cu$_2$O (sample B), Pt/TiO$_2$/Cu$_2$O/AuNPs (sample C), Pt/TiO$_2$/Cu$_2$O/NiO (sample D), and Pt/TiO$_2$/Cu$_2$O/NiO/AuNPs (sample E), respectively.

Figure 7(c) shows the hydrogen yields of Pt/TiO$_2$, Pt/TiO$_2$/Cu$_2$O, Pt/TiO$_2$/Cu$_2$O/AuNPs, Pt/TiO$_2$/Cu$_2$O/NiO and Pt/TiO$_2$/Cu$_2$O/NiO/AuNPs, which are tested at -0.18 V vs. RHE under the continuous irradiation for 2 h. The stability test of Pt/TiO$_2$/Cu$_2$O/NiO/AuNPs is shown in Figure S12a, and its hydrogen production is confirmed by the observation that bubbles are formed quickly and then leave off the photoelectrode surface immediately (see Figure S12b and the video in Visualization 1). Figure 7(d) plots and compares the measured results of different photocathodes. The hydrogen production rate of the Pt/TiO$_2$/Cu$_2$O/NiO/AuNPs photoelectrode (16.4 μmol·cm^{-2}·h^{-1}) is much higher than those of Pt/TiO$_2$ (1.43 μmol·cm^{-2}·h^{-1}), Pt/TiO$_2$/Cu$_2$O (4.42 μmol·cm^{-2}·h^{-1}), Pt/TiO$_2$/Cu$_2$O/AuNPs (10.5 μmol·cm^{-2}·h^{-1}) and Pt/TiO$_2$/Cu$_2$O/NiO (7.78 μmol·cm^{-2}·h^{-1}). The higher rate of hydrogen evolution corresponds to the larger magnitude of photocurrent in Fig. 7(a). By adopting the narrow-bandgap p-type Cu$_2$O, the Pt/TiO$_2$/Cu$_2$O heterojunction shows a higher hydrogen production rate due to the enhanced absorption in visible light and the formed p-n junction that promotes the electron-hole separation. As the AuNPs have a strong SPR effect in the visible light region, Pt/TiO$_2$/Cu$_2$O/AuNPs and Pt/TiO$_2$/Cu$_2$O/NiO/AuNPs exhibit an obvious enhancement of hydrogen production rate compared with Pt/TiO$_2$/Cu$_2$O (i.e., 10.5 and 16.4 versus 4.42 μmol·cm^{-2}·h^{-1}). The effectiveness of the NiO thin film as the HTL to improve the separation of charge carriers is verified by the higher performance of Pt/TiO$_2$/Cu$_2$O/NiO than Pt/TiO$_2$/Cu$_2$O (i.e., 7.78 versus 4.42 μmol·cm^{-2}·h^{-1}). Thanks to the synergistic effect of the NiO film's promotion of the electron-hole separation and the PIRET effect's excitation of more charge carriers in Cu$_2$O, the Pt/TiO$_2$/Cu$_2$O/NiO/AuNPs multilayer shows the best water splitting performance.

4. Conclusions

To make better use of the full-spectrum solar light for the PEC water splitting, we have presented a Pt/TiO$_2$/Cu$_2$O/NiO/AuNPs multilayered photocathode that enables the PIRET effect by the AuNPs and the unidirectional transport of photo-excited charge carriers by the NiO HTL layer. Furthermore, the TiO$_2$/Cu$_2$O heterostructure absorbs both the visible and UV lights and forms a p-n junction to promote the electron-hole separation; the TiO$_2$ coverage protects the underneath layers from electrochemical corrosion. With these favourable features, our Pt/TiO$_2$/Cu$_2$O/NiO/AuNPs photocathode yields the photocurrent -1.44 mA·cm^{-2} at the bias of -0.18 V vs. RHE, the ABPE of 1.5% and the hydrogen production rate of 16.4 μmol·cm^{-2}·h^{-1}. In addition, the contribution of plasmonic effects is also verified by numerical simulations. This study represents the first use of the NiO HTL as the spacer to enable the PIRET effect and to suppress the DET effect and the LEMF effect. It shows that the PIRET effect itself already works well for plasmonic enhancement of solar water splitting, and it would provide one more mechanism for designing energy-efficient PEC cells, photocatalysis and photovoltaics using solar light.

Disclosures. The authors declare no conflicts of interest.

Data availability. Data underlying the results presented in this paper are not publicly available at this time but may be obtained from the authors upon reasonable request.

Supplemental document. See Supplement 1 for supporting content.

References

1. C. G. Morales-Guio, S. D. Tilley, H. Vrubel, M. Grätzel, and X. Hu, "Hydrogen evolution from a copper(I) oxide photocathode coated with an amorphous molybdenum sulphide catalyst," Nat. Commun. **5**(I), 1–7 (2014).
2. Y. Wei, X. Chang, T. Wang, C. Li, and J. Gong, "A Low-Cost NiO Hole Transfer Layer for Ohmic Back Contact to Cu$_2$O for Photoelectrochemical Water Splitting," Small **13**(39), 1–7 (2017).
3. L. Sinatra, A. P. Lagrow, W. Peng, A. R. Kirmani, A. Amassian, H. Idriss, and O. M. Bakr, "A Au/Cu$_2$O-TiO$_2$ system for photo-catalytic hydrogen production. A pn-junction effect or a simple case of in situ reduction?" J. Catal. **322**, 109–117 (2015).
4. A. Fujishima and K. Honda, "Electrochemical photolysis of water at a semiconductor electrode," Nature **238**(5358), 37–38 (1972).
5. M. G. Walter, E. L. Warren, J. R. McKone, S. W. Boettcher, Q. Mi, E. A. Santori, and N. S. Lewis, "Solar Water Splitting Cells," Chem. Rev. **110**(11), 6446–6473 (2010).
6. W. Siripala, A. Ivanovskaya, T. F. Jaramillo, S. H. Baeck, and E. W. McFarland, "A Cu$_2$O/TiO$_2$ heterojunction thin film cathode for photoelectrocatalysis," Sol. Energy Mater. Sol. Cells **77**(3), 229–237 (2003).
7. P. Peerakiatkhajohn, T. Butburee, J.-H. Yun, H. Chen, R. M. Richards, and L. Wang, "A hybrid photoelectrode with plasmonic Au@TiO$_2$ nanoparticles for enhanced photoelectrochemical water splitting," J. Mater. Chem. A **3**(40), 20127–20133 (2015).
8. J. H. Yun, Y. H. Ng, C. Ye, A. J. Mozer, G. G. Wallace, and R. Amal, "Sodium fluoride-assisted modulation of anodized TiO$_2$ nanotube for dye-sensitized solar cells application," ACS Appl. Mater. Interfaces **3**(5), 1585–1593 (2011).
9. J. Gan, X. Lu, and Y. Tong, "Towards highly efficient photoanodes: Boosting sunlight-driven semiconductor nanomaterials for water oxidation," Nanoscale **6**(13), 7142–7164 (2014).
10. S.-Y. Fu, Y.-K. Hsu, M.-H. Chen, C.-J. Chuang, Y.-C. Chen, and Y.-G. Lin, "Silver-decorated hierarchical cuprous oxide micro/nanospheres as highly effective surface-enhanced Raman scattering substrates," Opt. Express **22**(12), 14617 (2014).
11. A. Paracchino, V. Laporte, K. Sivula, M. Grätzel, and E. Thimsen, "Highly active oxide photocathode for photoelectrochemical water reduction," Nat. Mater. **10**(6), 456–461 (2011).

12. J. Azevedo, S. D. Tilley, M. Schreier, M. Stefik, C. Sousa, J. P. Araújo, A. Mendes, M. Grätzel, and M. T. Mayer, "Tin oxide as stable protective layer for composite cuprous oxide water-splitting photocathodes," Nano Energy **24**, 10–16 (2016).

13. M. Alqahtani, S. Ben-Jabar, M. Ebaid, S. Sathasivam, P. Jurczak, X. Xia, A. Alromaeh, C. Blackman, Y. Qin, B. Zhang, B. S. Ooi, H. Liu, I. P. Parkin, and J. Wu, "Gallium Phosphide photoanode coated with TiO_2 and CoO_x for stable photoelectrochemical water oxidation," Opt. Express **27**(8), A364 (2019).

14. X. Zhang, Y. L. Chen, R.-S. Liu, and D. P. Tsai, "Plasmonic photocatalysis," Reports Prog. Phys. **76**(4), 046401 (2013).

15. F. Tan, N. Wang, D. Y. Lei, W. Yu, and X. Zhang, "Plasmonic Black Absorbers for Enhanced Photocurrent of Visible-Light Photocatalysis," Adv. Opt. Mater. **5**(2), 600399 (2017).

16. K. H. W. Ho, A. Shang, F. Shi, T. W. Lo, P. H. Yeung, Y. S. Yu, X. Zhang, K. yin Wong, and D. Y. Lei, "Plasmonic Au/TiO_2-Dumbbell-On-Film Nanocavities for High-Efficiency Hot-Carrier Generation and Extraction," Adv. Funct. Mater. **28**(34), 1–10 (2018).

17. H. Jia, Y. L. Wong, A. Jian, C. C. Tsoi, M. Wang, W. Li, W. Zhang, S. Sang, and X. Zhang, "Microfluidic reactors for plasmonic photocatalysis using gold nanoparticles," Micromachines **10**(12), 869 (2019).

18. S. K. Cushing, J. Li, F. Meng, T. R. Senty, S. Suri, M. Zhi, M. Li, A. D. Bristow, and N. Wu, "Photocatalytic Activity Enhanced by Plasmonic Resonant Energy Transfer from Metal to Semiconductor," J. Am. Chem. Soc. **134**(36), 15033–15041 (2012).

19. J. Li, S. K. Cushing, P. Zheng, F. Meng, D. Chu, and N. Wu, "Plasmon-induced photonic and energy-transfer enhancement of solar water splitting by a hematite nanorod array," Nat. Commun. **4**, 2651 (2013).

20. P. A. Desario, J. J. Pietron, D. E. Devantier, T. H. Brintlinger, R. M. Stroud, and D. R. Rolison, "Plasmonic enhancement of visible-light water splitting with $Au-TiO_2$ composite aerogels," Nanoscale **5**(17), 8073–8083 (2013).

21. P. S. Archana, N. Pachauri, Z. Shan, S. Pan, and A. Gupta, "Plasmonic Enhancement of Photoactivity by Gold Nanoparticles Embedded in Hematite Films," J. Phys. Chem. C **119**(27), 15506–15516 (2015).

22. M. M. Abouelela, G. Kawamura, and A. Matsuda, "A review on plasmonic nanoparticle-semiconductor photocatalysts for water splitting," J. Clean. Prod. **294**, 126200 (2021).

23. A. Primo, A. Corma, and H. García, "Titania supported gold nanoparticles as photocatalyst," Phys. Chem. Chem. Phys. **13**(3), 886–910 (2011).

24. D. A. Panayotov and J. R. Morris, "Surface chemistry of Au/TiO_2: Thermally and photolytically activated reactions," Surf. Sci. Rep. **71**(1), 77–271 (2016).

25. Z. Lin, X. Wang, J. Liu, Z. Tian, L. Dai, B. He, C. Han, Y. Wu, Z. Zeng, and Z. Hu, "On the role of localized surface plasmon resonance in UV-Vis light irradiated Au/TiO_2 photocatalysis systems: Pros and cons," Nanoscale **7**(9), 4114–4123 (2015).

26. G. Kawamura and A. Matsuda, "Synthesis of plasmonic photocatalysts for water splitting," Catalysts **9**(12), 982 (2019).

27. B. Ma, J. Bi, J. Lv, C. Kong, P. Yan, X. Zhao, X. Zhang, T. Yang, and Z. Yang, "Inter-embedded $Au-Cu_2O$ heterostructure for the enhanced hydrogen production from water splitting under the visible light," Chem. Eng. J. **405**, 126709 (2021).

28. D. Chen, Z. Liu, Z. Guo, W. Yan, and Y. Xin, "Enhancing light harvesting and charge separation of Cu_2O photocathodes with spatially separated noble-metal cocatalysts towards highly efficient water splitting," J. Mater. Chem. A **6**(41), 20393–20401 (2018).

29. C.-Y. Lin, Y.-H. Lai, D. Mersch, and E. Reisner, "$Cu2O|NiOx$ nanocomposite as an inexpensive photocathode in photoelectrochemical water splitting," Chem. Sci. **3**(12), 3482 (2012).

30. J. Li, S. K. Cushing, F. Meng, T. R. Senty, A. D. Bristow, and N. Wu, "Plasmon-induced resonance energy transfer for solar energy conversion," Nat. Photonics **9**(9), 601–607 (2015).

31. X. Wang, R. Long, D. Liu, D. Yang, C. Wang, and Y. Xiong, "Enhanced full-spectrum water splitting by confining plasmonic Au nanoparticles in N-doped TiO_2 bowl nanoarrays," Nano Energy **24**, 87–93 (2016).

32. H. Robatjazi, S. M. Bahauddin, C. Doiron, and I. Thomann, "Direct Plasmon-Driven Photoelectrocatalysis," Nano Lett. **15**(9), 6155–6161 (2015).

33. A. A. Al-Ghamdi, W. E. Mahmoud, S. J. Yaghmour, and F. M. Al-Marzouki, "Structure and optical properties of nanocrystalline NiO thin film synthesized by sol-gel spin-coating method," J. Alloys Compd. **486**(1-2), 9–13 (2009).

34. M. M. Hasan, A. S. M. A. Haseeb, R. Saidur, and H. H. Masjuki, "Effects of annealing treatment on optical properties of anatase TiO_2 thin films," World Acad. Sci. Eng. Technol. **40**, 221–225 (2009).

35. C. Xiang, G. M. Kimball, R. L. Grimm, B. S. Brunschwig, H. A. Atwater, and N. S. Lewis, "820 mV open-circuit voltages from Cu_2O/CH_3CN junctions," Energy Environ. Sci. **4**(4), 1311–1318 (2011).

36. S. C. Roy, O. K. Varghese, M. Paulose, and C. A. Grimes, "Toward solar fuels: Photocatalytic conversion of carbon dioxide to hydrocarbons," ACS Nano **4**(3), 1259–1278 (2010).

37. D. Saranin, P. Gostischev, D. Tatarinov, I. Ermanova, V. Mazov, D. Muratov, A. Tameev, D. Kuznetsov, S. Didenko, and A. Di Carlo, "Copper Iodide Interlayer for Improved Charge Extraction and Stability of Inverted Perovskite Solar Cells," Materials **12**(9), 1406 (2019).

38. J. P. Yasomanee and J. Bandara, "Multi-electron storage of photoenergy using Cu_2O-TiO_2 thin film photocatalyst," Sol. Energy Mater. Sol. Cells **92**(3), 348–352 (2008).

39. Y. K. Hsu, C. H. Yu, Y. C. Chen, and Y. G. Lin, "Synthesis of novel Cu_2O micro/nanostructural photocathode for solar water splitting," Electrochim. Acta **105**, 62–68 (2013).

40. D. Wang, X. Pan, G. Wang, and Z. Yi, "Improved propane photooxidation activities upon nano Cu_2O/TiO_2 heterojunction semiconductors at room temperature," RSC Adv. **5**(28), 22038–22043 (2015).

41. V. V. Pham, D. P. Bui, H. H. Tran, M. T. Cao, T. K. Nguyen, Y. S. Kim, and V. H. Le, "Photoreduction route for Cu_2O/TiO_2 nanotubes junction for enhanced photocatalytic activity," RSC Adv. **8**(22), 12420–12427 (2018).

42. W. Li and F. Jäckel, "Size-controlled electron transfer rates determine hydrogen generation efficiency in colloidal Pt-decorated CdS quantum dots," Nanoscale **10**(34), 16153–16158 (2018).

43. Y. Park, J. Choi, C. Lee, A. N. Cho, D. W. Cho, N. G. Park, H. Ihee, and J. Y. Park, "Elongated Lifetime and Enhanced Flux of Hot Electrons on a Perovskite Plasmonic Nanodiode," Nano Lett. **19**(8), 5489–5495 (2019).

44. Z. Hu, Y. Mi, Y. Ji, R. Wang, W. Zhou, X. Qiu, X. Liu, Z. Fang, and X. Wu, "Multiplasmon modes for enhancing the photocatalytic activity of $Au/Ag/Cu_2O$ core-shell nanorods," Nanoscale **11**(35), 16445–16454 (2019).

45. D. Liang, G. Han, Y. Zhang, S. Rao, S. Lu, H. Wang, and Y. Xiang, "Efficient H_2 production in a microbial photoelectrochemical cell with a composite Cu_2O/NiO_x photocathode under visible light," Appl. Energy **168**, 544–549 (2016).

46. Z. Li and Z. Zhang, "Tetrafunctional Cu_2S thin layers on Cu_2O nanowires for efficient photoelectrochemical water splitting," Nano Res. **11**(3), 1530–1540 (2018).

47. S. Masudy-Panah, R. Siavash Moakhar, C. S. Chua, H. R. Tan, T. I. Wong, D. Chi, and G. K. Dalapati, "Nanocrystal Engineering of Sputter-Grown CuO Photocathode for Visible-Light-Driven Electrochemical Water Splitting," ACS Appl. Mater. Interfaces **8**(2), 1206–1213 (2016).

48. L. Liu, G. Wang, Y. Li, Y. Li, and J. Z. Zhang, "CdSe quantum dot-sensitized Au/TiO_2 hybrid mesoporous films and their enhanced photoelectrochemical performance," Nano Res. **4**(3), 249–258 (2011).

49. K. C. Kao, Y. Kuroiwa, H. Nishi, and T. Tatsuma, "Hydrogen evolution from water based on plasmon-induced charge separation at a $TiO_2/Au/NiO/Pt$ system," Phys. Chem. Chem. Phys. **19**(46), 31429–31435 (2017).

50. Z. Zhang, R. Dua, L. Zhang, H. Zhu, H. Zhang, and P. Wang, "Carbon-layer-protected cuprous oxide nanowire arrays for efficient water reduction," ACS Nano **7**(2), 1709–1717 (2013).

51. Y. Yue, P. Zhang, W. Wang, Y. Cai, F. Tan, X. Wang, X. Qiao, and P. K. Wong, "Enhanced dark adsorption and visible-light-driven photocatalytic properties of narrower-band-gap Cu_2S decorated Cu_2O nanocomposites for efficient removal of organic pollutants," J. Hazard. Mater. **384**, 121302 (2020).

52. S. K. Mohapatra, M. Misra, V. K. Mahajan, and K. S. Raja, "Design of a highly efficient photoelectrolytic cell for hydrogen generation by water splitting: Application of $TiO_{2-x}C_x$ nanotubes as a photoanode and Pt/TiO_2 nanotubes as a cathode," J. Phys. Chem. C **111**(24), 8677–8685 (2007).

53. X. L. Du, X. L. Wang, Y. H. Li, Y. L. Wang, J. J. Zhao, L. J. Fang, L. R. Zheng, H. Tong, and H. G. Yang, "Isolation of single Pt atoms in a silver cluster: Forming highly efficient silver-based cocatalysts for photocatalytic hydrogen evolution," Chem. Commun. **53**(68), 9402–9405 (2017).